university of groningen / faculty of science and engineering / biomedical engineering

Experimental and Pre-clinical Evaluation of Reconstruction Methods in Dynamic PET: Quantitative Characteristics and Effects on Kinetic Modelling

Valentina Turmacu

S4317114

Department of Nuclear Medicine and Molecular Imaging

Period: 18/04/2023 - 01/07/2023

Bachelor's project

1st Examiner: prof. dr. ir. Charalampos Tsoumpas, Department of Nuclear Medicine and Molecular Imaging

2nd Examiner: dr. Antoon Willemsen, Department of Nuclear Medicine and Molecular Imaging

Daily supervisor: Giordana Salvi de Souza

Contents

Abstract

Positron emission tomography (PET) is a widely used imaging technique that generates molecular images reflecting physiological processes in human and animal tissues. PET images can be acquired statically or dynamically, with dynamic acquisition providing information about radiotracer kinetics. The choice of a reconstruction algorithm in PET affects the accuracy of quantitative measurements and image interpretation. Filtered back projection (FBP) is a fast and reliable algorithm but may result in poor image quality and a low signal-to-noise ratio. Iterative algorithms like ordered-subset expectation maximization (OSEM) can overcome these limitations but may introduce biases in reconstructed activity concentration, particularly in cold regions, leading to errors in derived biological parameters. This study aimed to evaluate the effects of reconstruction algorithms on image quality and activity concentration in both phantom and animal settings. The NEMA NU 4–2008 image quality phantom was used to assess FBP2D, RP3D, and OSEM2D reconstruction methods for the Siemens microPET Focus 220 scanner. Additionally, pre-clinical data using the [^{18}F]MC225 radiotracer was evaluated with the same reconstruction algorithms to assess their performance in a real-world scenario. Image quality metrics like recovery coefficient, activity concentration, noise, and spillover ratio were extracted from the phantom scans and analyzed to establish a golden standard reconstruction method. The [^{18}F]MC225 rat data study involved brain dynamic PET scans, blood sample collection, and analysis using kinetic modeling. Tissue time-activity curves (TACs) were obtained, and the 1-tissue compartment model (1TCM) was used to determine kinetic parameters like total distribution volume (V_T), uptake rate constant (K_1), and clearance rate constant (k_2). The phantom study showed that OSEM2D* (routine protocol) performed best across the multiple image quality metrics and frame durations (static, dynamic 120 seconds, dynamic 30 seconds), the priority metric being activity concentration percentage error. OSEM2D was found to perform very similarly. The [^{18}F]MC225 study showed that no significant differences were found between the TACs across the reconstruction methods and some significant differences were found across the kinetic parameters for one study subject. However, the model fit analysis showed that 1TCM fit best on OSEM2D* reconstructed images, both by the standard error of the estimated kinetic parameters and the Akaike information criterion. Limitations were observed in the sample size of the animal study and the lack of biodistribution data, which would help validate the microPET values in similar future studies. Moreover, it would be relevant to conduct a similar phantom and animal study with different reconstruction methods and radiotracers.

1 Introduction

Positron emission tomography (PET) is an imaging modality widely used in clinical and research. It enables the generation of molecular images that reflect physiological processes in human and animal tissues and organs [1]. The technique evaluates the three-dimensional spatial distribution of tracers that incorporate positron-emitting radioactive isotopes. The most commonly used radioisotopes in PET imaging are fluorine-18 (^{18}F), carbon-11 (^{11}C), nitrogen-13 (^{13}N), gallium-68 (^{68}Ga), zirconium-89 (^{89}Zr), and oxygen-15 (^{15}O), with half-lives ranging from two minutes to 3.3 days. By labeling various molecules, such as drugs and pharmaceuticals, it is possible to assess parameters such as glucose metabolic rate, transporters, receptors, and myocardial oxygen consumption, among others, to gain insights into physiological processes [2–4].

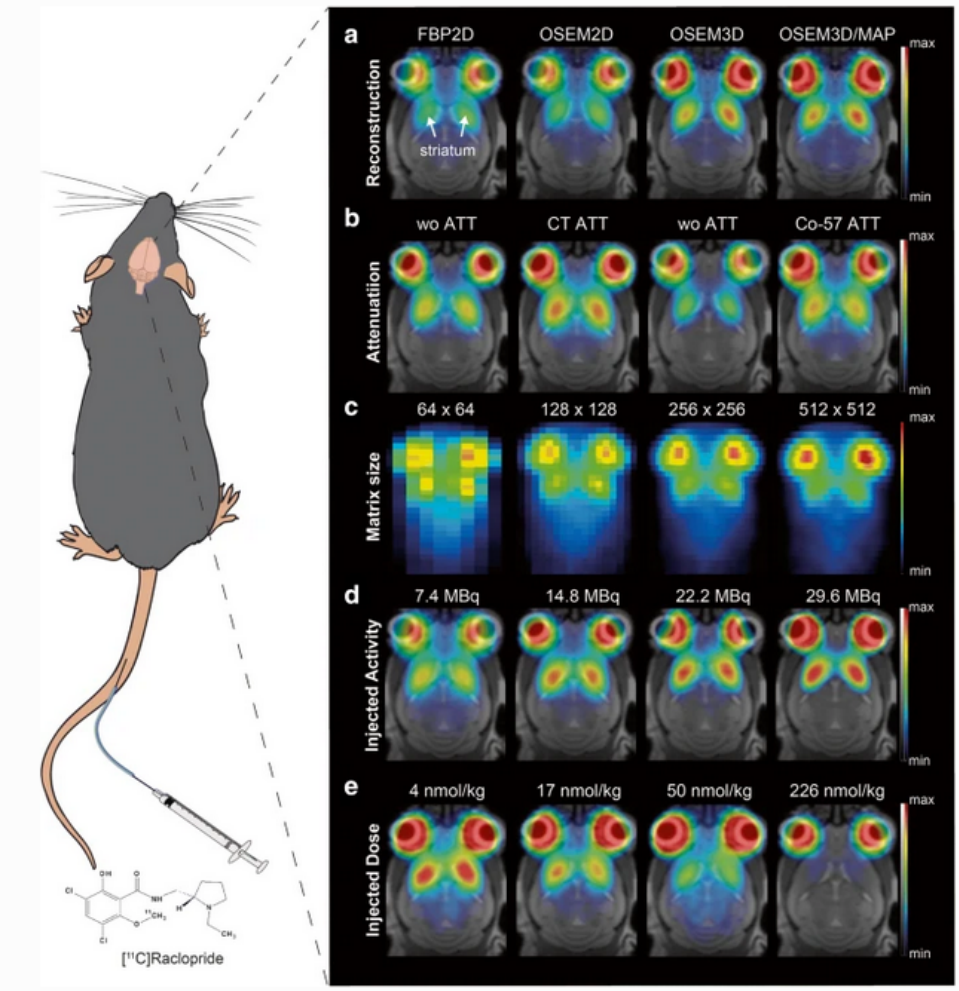

Fig. 1. Comparison of [^{11}C]raclopride mouse brain PET images using different 2D and 3D reconstruction algorithms (a), CT versus Co-57 attenuation correction (b), increasing matrix sizes (c), increasing injected activity (d), and increasing injected doses (e)[5].

MicroPET systems play a crucial role in preclinical research by enabling the study of molecular processes in small animals. These systems offer higher spatial resolution and sensitivity compared to clinical PET scanners, allowing researchers to investigate dynamic changes at the molecular level in animal models of diseases. The use of microPET in research provides several advantages [6, 7].

Firstly, it allows for the non-invasive longitudinal monitoring of disease progression, response to therapy, and the development of new drugs. Researchers can track the spatiotemporal distribution of radiotracers in animal models over time, providing valuable insights into the underlying biological processes. Furthermore, PET imaging permits the same experiments in rodents, non-human primates, and humans, enabling longitudinal studies and facilitating translations between basic and clinical research (see Figure 1) [8–11].

While dynamic PET and radiotracer kinetics quantification provide important information about physiological and biochemical processes [12], several factors can influence the accuracy of quantitative measurements and image interpretation in PET [13]. One such factor is the choice of a reconstruction algorithm. Analytic or iterative algorithms can be employed to reconstruct the activity map for each time frame. Filtered back projection (FBP) is a fast and reliable algorithm for quantitative results. However, it may lead to poor image quality in PET data due to streak artifacts and a low signal-to-noise ratio (SNR) in cases with limited statistics [14, 15]. Iterative reconstruction algorithms, such as ordered-subset expectation maximization (OSEM), can overcome these limitations. However, iterative algorithms may introduce biases in reconstructed activity concentration, as a result of non-negativity constraints, particularly in cold regions. This bias can potentially lead to errors in the derived biological parameters from dynamic PET images [12].

Therefore, the goal of this study was to evaluate the effects of the reconstruction algorithm on image quality and activity concentration in a phantom and animal setting. The NEMA NU 4–2008 image quality phantom was used to assess the following reconstruction methods: 2D filtered back projection (FBP), 3D re-projection (RP3D), and 2D ordered-subset expectation maximization (OSEM2D), with the aim of establishing the best reconstruction method for the Siemens microPET Focus 220 scanner [16]. Additionally, [^{18}F]MC225 pre-clinical data was evaluated using the same reconstruction algorithms to evaluate their performance in a real-world scenario and address the effects of reconstruction methods on quantitative PET analysis methods.

1.1 Theoretical Background

1.1.1 PET radionuclides

PET is an imaging technique that utilizes detection probes labeled with positron-emitting radionuclides to visualize human physiology at the molecular level. These radiotracers provide detectable signals and they can be formulated as tissue-specific or receptor-specific, targeting the structures or physiological processes being studied. One advantage of PET is that a part of the positron emitting isotopes have low atomic mass elements, a preferred trait ensuring minimum interference with the biological activity of the tracers [17]. ^{18}F is the most commonly used radionuclide due to its convenient half-life of $T_{1/2} = 109.8$ minutes, the simple substitution needed to develop active fluoro-organic drugs, and improved count statistics. Substituting a hydrogen atom with an ^{18}F atom frequently does not affect the size or shape of the tracer and produces metabolically stable compounds [17, 18].

[^{18}F]FDG. The reliable fabrication of [^{18}F]FDG has made PET imaging critical in clinical nuclear medicine through its role in energy metabolism studies and metastatic cancer site detection. As the most used PET pharmaceutical, [^{18}F]FDG is present in roughly 95% of all clinical oncology PET studies [17, 19].

[^{18}F]MC225. P-glycoprotein (P-gp) is an ATP-binding cassette transporter located in the luminal membrane of the blood-brain barrier (BBB). P-gp has a protective role for the brain tissue against hydrophobic xenobiotics, but it can also limit the access of antiepileptics, antidepressants, and anticancer drugs to the brain target sites [20]. Furthermore, P-gp function is found to be related to neurological diseases such as Alzheimer's and Parkinson's disease. In both diseases, reduced P-gp activity is seen at the BBB and it facilitates the growth of toxic compounds in the brain [20, 21].

When analysing P-gp activity using PET imaging, (R)-[^{11}C]verapamil is the most commonly used radiotracer. However, it is not an ideal one due to its sub-optimal lipophilicity and metabolite profile [18]. Moreover, (R)-[^{11}C]verapamil can only visualise decreases in P-gp function and not increases as well and has poor sensitivity to small changes of the P-gp function [21].

The novel tracer [^{18}F]MC225 is a weaker P-gp substrate and it has exhibited higher brain uptake values at baseline condition compared with (R)-[^{11}C]verapamil, allowing for measurement of both increases and decreases of P-gp function [18, 21]. Additionally, the cardiovascular safety of this radiotracer has been shown by Fusi et al. as MC225-induced cardiovascular effects occurred at administered concentrations at least 100 times greater than the necessary doses for P-gp imaging [20].

1.1.2 Acquisition methods

PET images can be acquired statically or dynamically (see Figure 2). In static acquisition, it is necessary to specify a time period throughout the acquisition. The result is a single frame representing the average amount of radioactivity during the acquisition period [22]. In dynamic acquisition, it is possible to observe the behavior of the radiotracer uptake in the tissue of interest over time. The image acquisition starts along with the administration of the radiotracer so that the whole imaging time, from the beginning, is present in the acquisition [23].

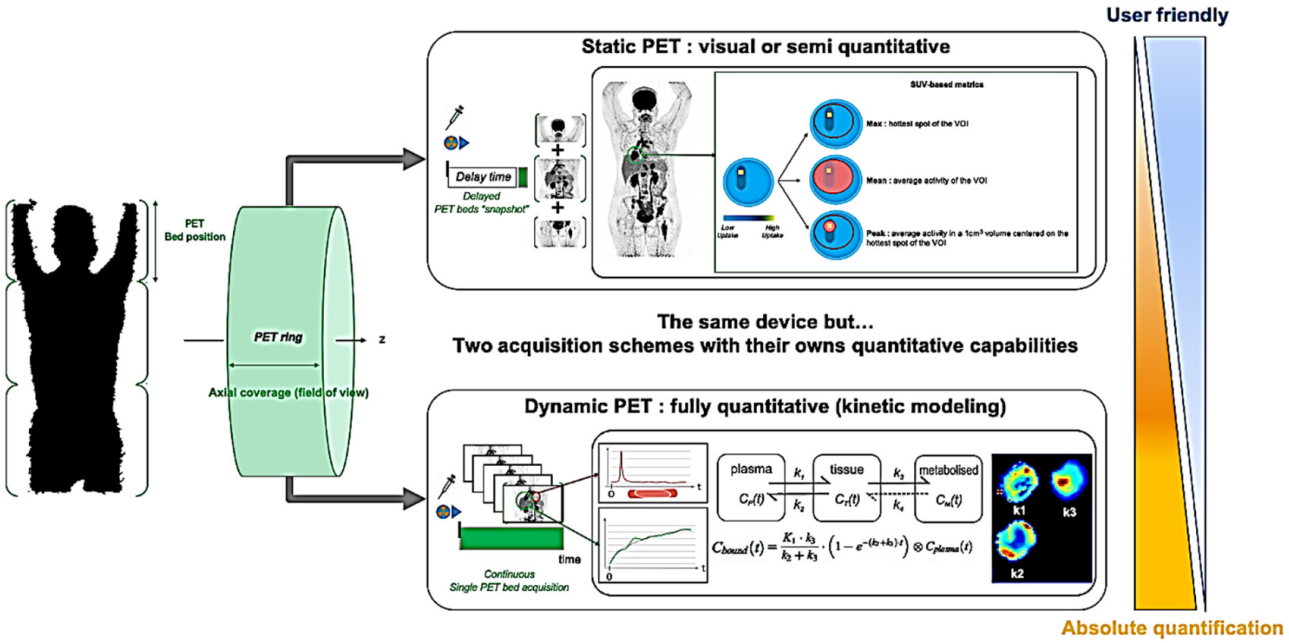

Fig. 2. Schematic representation of PET [24].

1.1.3 Reconstruction methods

Filtered backprojection (FBP) was the first reconstruction algorithm used and it continues to provide accurate 2D radiotracer distributions when applied to noise free projection data. Due to its mathematical simplicity, it is easy to implement and fast to reconstruct. However, the ramp filter, which is used to remove star artifacts and enhance spatial resolution, can amplify noise, especially in low counts images [25].

Re-projection (RP), more specifically RP3D, is considered the standard reconstruction method of truncated 3D PET data and it is based on the fact that 2D data is sufficient for reconstructions. RP3D estimates the unmeasured data by calculating the line integrals along the lines of response (LORs), thus improving the statistical properties of the images by utilising additional data [17, 26]. However, it is known that the image variance is chiefly influenced by the smoothing effect inherent in the RP3D algorithm. Because the truncated data is obtained by forward projecting the initial image estimate reconstructed from the 2D data subset, data with lower variance compared to the measured data is generated. This smoothing effect is increased in regions with higher use of estimated data [26].

Ordered subset expectation maximization (OSEM) is an iterative algorithm that produces images of higher visual quality compared to FBP, particularly in low count images. In regards to noise, OSEM generally produces less noisy images with improved artifact reduction compared to FBP, due to its iterative nature. However, higher numbers of iterations also lead to significantly longer processing times, potential noise amplification, and image quality deterioration [25, 27]. Thus, with the correct number of iterations, OSEM can produce higher quantitative accuracy especially when reconstructing noisy images. An additional disadvantage of all nonlinear algorithms such as OSEM is the spatially variant and object-dependent convergence properties which may lead to incompletely converged images, especially in noisy images [25, 28]. A method used to overcome the limit cycle of OSEM in noisy data is reducing the number of subsets which in turn will slow down the convergence [17]. Thus, the best reconstruction method to use on noisy images remains to be studied. Lastly, activity overestimations in cold areas may arise when using OSEM due the non-negativity constraint of the voxel values [29]

When evaluating reconstruction methods, it is important to take into account the goal of the images as Boellard et al. have found that FBP and OSEM produce similar results for most PET studies, however, OSEM does not perform as accurately when conducting FDG cardiac PET studies [30]. Similarly, Shi et al. have found that OSEM is less reliable in cardiac [^{11}C]acetate kinetic analysis studies [31].

2D and 3D reconstructions significantly differ in terms of image quality due to their data processing methods. In 2D reconstructions, each projection angle is reconstructed independently and added to form a 3D image volume, leading to lower image quality and potential for interpolation artifacts, whereas 3D reconstruction uses all data from all angles simultaneously. In 3D projection data, each LOR's axial angle is taken into account leading to tremendous volumes of data to process. Thus, improved image quality comes at the cost of longer computation times and the need for larger memory and processing power [25].

1.1.4 PET quantification methods

PET quantitative approaches may be classified into three categories: qualitative methods such as visual assessment, semiquantitative methods such as standardised uptake value (SUV), and absolute

methods such as kinetic modelling analysis [17]. When applying the aforementioned quantitative approaches, the critical starting points are not the models applied but the PET camera measurements, often expressed as time activity curves (TACs), and the blood data, extracted from arterial blood samples or image-derived using reference regions of interest (ROIs) with no specific uptake [32].

Multiple general assumptions must be made before quantification [32]. Firstly, the physiological processes and molecular interactions are not affected by PET measurement. Secondly, the physiological processes and molecular interactions are in a constant state during the PET measurement. Lastly, when using compartment modelling, the concentration in the compartments is homogeneous [32].

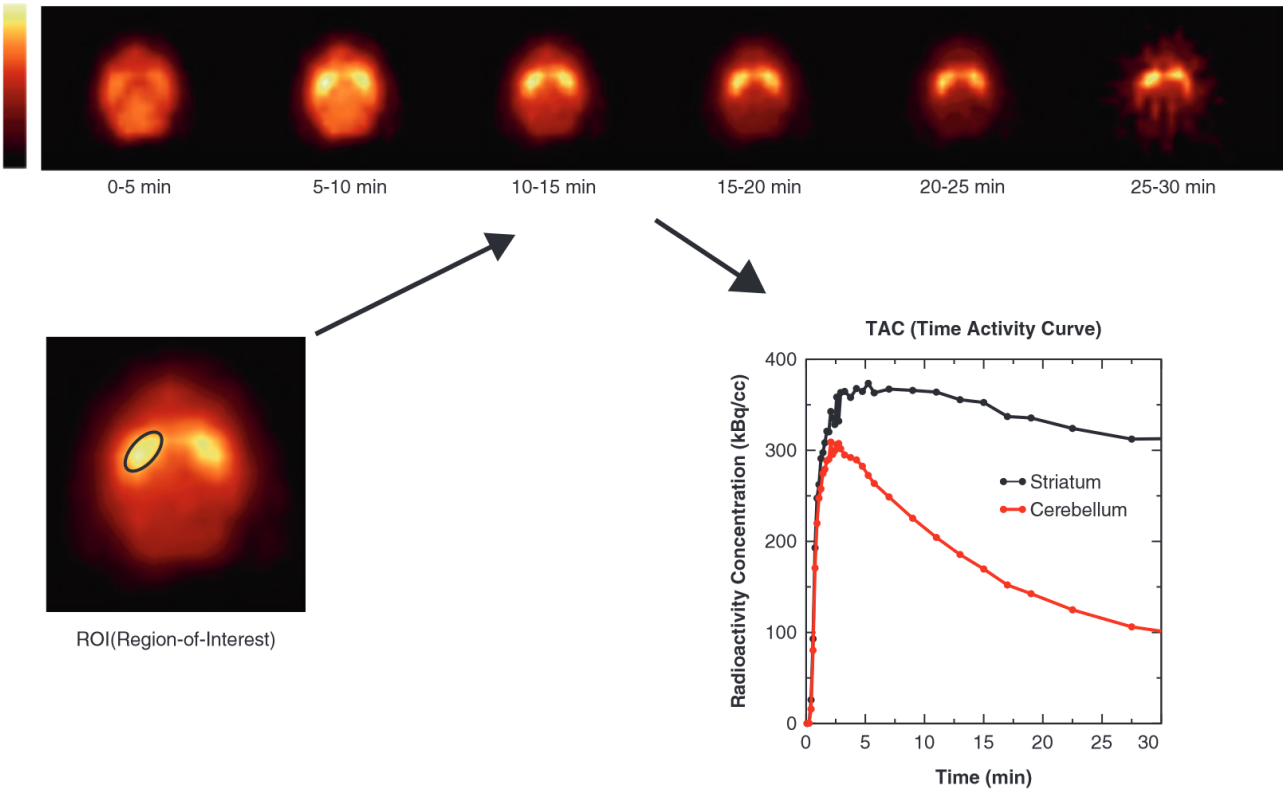

Fig. 3. Schematic of ROI TACs process [17].

1.1.5 Time activity curves (TACs)

In order to obtain temporal information such as time-activity curves, dynamic PET scans must be acquired. The most commonly used approach is the ROI TACs which extract the averaged activity concentration within a predefined ROI and plot it against the scan time (see Figure 3). Alternately, a voxel-based approach can be followed which results in parametric images. However, ROI TACs have significantly less noise than voxel TACs and the estimated kinetic parameters have a reduced variance. Due to the partial volume effect (PVE), an inhomogenous bias occurs in parametric imaging, as one voxel may include multiple types of cells with various functions [17]. The potential disadvantage of ROI TACs is the time-consuming process of delineating ROIs and the possibility of interobserver variability. Nonetheless, automatic ROI selections in brain images have been developed based on co-registrated PET images to atlas CT or MRI images [17]. One of the challenges posed by TACs is the frame duration selection, as it must ensure sufficient temporal resolution and statistically adequate counts [33].

1.1.6 Kinetic modelling

The main goal of PET kinetic modelling is to understand the relationship between tissue measurements and the underlying physiological processes, such as blood flow and metabolism. As previously mentioned, the measured TACs and the blood data are essential to tracer kinetic analysis. Due to P-gp being expressed throughout the brain, suitable reference ROIs for image-derived input functions are non-existent. Thus, accurate input functions have to be extracted from the arterial blood data. To ensure accuracy, the blood must be frequently sampled throughout the duration of the dynamic PET scans and the recorded radioactivities must be delay corrected by taking into account the time it takes the tracer to reach the target organ [17]. From the whole-blood samples, the whole-blood activity, the plasma activity, and the fraction metabolite activity can be extracted through centrifugation and high-pressure liquid chromatography [17, 21].

As kinetic modelling is highly sensitive to noise and bias, the optimal kinetic model should be chosen taking into account the chemical and physiological properties of the tracer, the target tissue and process, and model performance [33]. Thus, the kinetic model used to analyse the [^{18}F]MC225 rat study was the 1-tissue compartment model (1TCM), as recommended by a study of Savolainen et al. which compared multiple kinetic modelling approaches (1TCM, 2TCM, Logan plot) and selected the most stable and reasonably accurate method [34]. The 1TCM model is described by the following mass balance differential equation:

$$\frac{dC_t(t)}{dt} = K_1 C_a(t) - k_2 C_t(t) \tag{1}$$

where $C_a(t)$ is the input curve, $C_t(t)$ is the tissue activity concentration, K_1 is the uptake rate constant (expressed in mL/mL/min), and k_2 is the clearance rate constant (expressed in 1/min). The 1TCM model is also described by the following operational model curve:

$$C_{Model}(t) = (1 - v_B)C_t(t) + v_B C_B(t) \tag{2}$$

where $C_B(t)$ is the tracer concentration in the whole blood and v_B is the blood volume fraction [35]. The 1TC model only separates tissue uptake and washout, as all tracer is included in only one compartment C_1 (see Figure 4.)

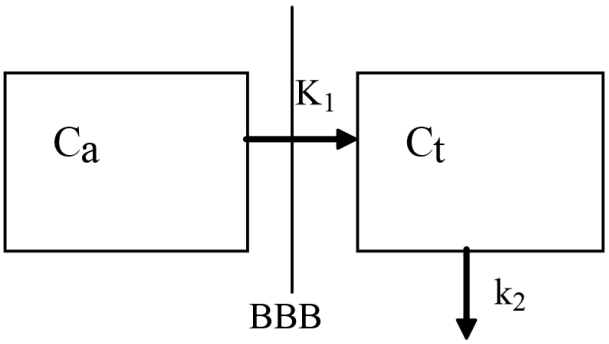

Fig. 4. 1-tissue compartment model (1TCM) [32].

When fitting the 1TCM model, the three variable parameters are v_B, K_1, and k_2, however, v_B is most often fixed at the physiological value. Savolainen et al. also determined that the most appropriate

blood volume fraction for such studies is 5% [34]. When the 1TCM model is applied in studies of P-gp activity at BBB, K_1 represents the unidirectional transport of radiotracer from plasma to compartment C_t. Another important parameter when comparing kinetic models is V_T, the ratio of radiotracer concentration in the target tissue and plasma at equilibrium, equal to K_1/k_2 [21, 35].

2 Materials and methods

2.1 System description

The PET images were obtained using a Siemens microPET Focus 220 scanner for small animals (Inveon, Siemens Medical Solutions, Malvern, PA, USA), which has 168 lutetium oxyorthosilicate (LSO) detector crystals (dimensions of 1.5 x 1.5 x 10 mm^3 each), a transaxial FOV of 19 cm, an axial FOV of 7.6 cm, and an absolute system sensitivity of 4%. The images were reconstructed using the microPET manager 2.4.1.1 software. Adjacent to the microPET scanner are the VDC 505 dose calibrator and the 2480 WIZARD 2 gamma counter [36, 37]. Both the animal scans and the phantom scans were acquired using the same microPET system.

2.2 Phantom study

It is highly relevant to evaluate the performance of the microPET scanner and its reconstruction methods in order to best analyse and compare the animal scans. Using the NU 4-2008 standards published by the National Electrical Manufacturers Association (NEMA), the overall image quality, accuracy, and precision of the scanner were characterised, and, using these metrics, a reconstruction golden standard was established [16].

2.2.1 NEMA NU 4–2008 image quality phantom

To determine the golden standard reconstruction method for the Siemens microPET Focus 220 scanner, the NEMA NU 4–2008 image quality (IQ) phantom was used. The phantom is made of polymethylmethacrylate (PMMA), it has an internal length of 50mm and an internal diameter of 30mm, and it is divided into 3 regions, as can be seen in Figure 5 [16, 38]. Each region was analysed to determine multiple metrics characterizing the image quality.

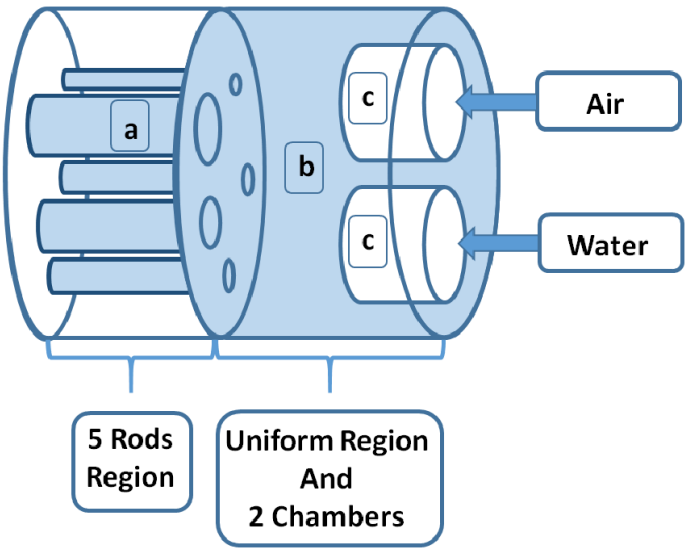

Fig. 5. microPET NEMA NU 4-2008 image quality phantom [38].

The first region, denoted in Figure 5 as the “5 rods region”, is used to determine the recovery coefficient (RC) and it consists of 5 fillable rods with diameters of 1, 2, 3, 4, and 5 mm [16]. The RC is

theoretically limited between 0 and 1 and is defined as:

$$\text{RC} = \frac{\text{activity concentration measured in the rods}}{\text{activity concentration measured in the uniform area}} \tag{3}$$

The uniform region is used to determine the mean, maximum, and minimum activity concentrations and the percentage standard deviation as a metric of noise [16]. Furthermore, the uniformity region was used to determine the percentage error of the activity, a key factor in establishing the golden standard reconstruction method, which was defined as:

$$\%\ \text{error} = \frac{\text{measured mean activity concentration} - \text{known activity concentration}}{\text{known activity concentration}} \tag{4}$$

Lastly, the spillover ratio (SOR) is used to evaluate the accuracy of corrections and is determined by analyzing the third region of the phantom which consists of two fillable cylindric chambers. One cold compartment was filled with air and the other with nonradioactive water. Both compartments have an internal length of 14mm and an inner diameter of 8mm [16]. Both cylinders are nonradioactive, however scattered photons, randoms, and other effects may cause activity in these areas [39]. Furthermore, the SOR is also theoretically limited between 0 and 1 and is defined as:

$$\text{SOR} = \frac{\text{activity concentration in cold region}}{\text{mean activity concentration in hot background}} \tag{5}$$

The process of determining the golden standard reconstruction method is highly dependent on finding the lowest error and noise.

2.2.2 Image acquisition procedure and Reconstruction methods

The NEMA IQ phantom was filled with a [^{18}F]FDG aqueous solution with an initial activity of 3.697 MBq and a known activity concentration of 179.87 kBq/cc. The radiotracer syringe was flushed multiple times to ensure there is as little as possible remaining activity. After that, the syringe was measured in the activity calibrator, and the remaining activity was recorded. The phantom was sealed and then agitated to obtain uniform radioactive solution distribution.

The phantom was scanned for 20 min, per standard NEMA NU 4 protocol, and a ^{57}Co transmission scan of 520 seconds was also conducted in order to determine the attenuation correction [16]. Prior to reconstruction, the 3D sinograms were rebinned using the Fourier algorithm. Normalization and scatter correction were applied to the data for all FBP2D, RP3D, and OSEM2D reconstructions. All reconstructions used the standard parameters recommended by the manufacturer (see Table 1). Additionally, a routine protocol OSEM2D reconstruction was performed and analysed, from now on referred to as OSEM2D*.

It should be noted that most literature conducts image quality testing on the microPET NEMA IQ phantom by reconstructing the images with additional algorithms, such as FBP3D, OSEM3D, and MLEM, and diverse filtering methods, such as Gaussian filters of different dimensions. Furthermore, many of the studies which use OSEM also analyse the effects the number of iterations and the number of subsets have on the image quality [39–47]. However, these reconstruction options could not be explored in this research as the scanner's software does not have the option to reconstruct MLEM and FBP3D. Furthermore, OSEM3D reconstructions were attempted, but due to the low processing power, all failed, and the number of subsets in the OSEM2D reconstruction could not be changed from 16.

Table 1. Applied reconstruction protocols. *Routine protocol performed.

	FBP2D	**RP3D**	**OSEM2D**	**OSEM2D***
Sinogram rebining algorithm	Fourier	Full 3D binning (span and ring difference)	Fourier	Fourier
Filter	Ramp (cutoff at Nyquist frequency)	None	Ramp (cutoff at Nyquist frequency)	Ramp (cutoff at Nyquist frequency)
Image matrix size	128 x 128	128 x 128	128 x 128	256 x 256
Pixel size (mm)	1.898	1.898	1.898	0.633
Slice thickness (mm)	0.796	0.796	0.796	0.796
Attenuation correction	Yes, using the point source singles form the transmission scan			
Scatter correction	Yes, direct calculation from analytical formulas			
Resolution (pixels per mm)	0.5268	0.5268	0.5268	1.5805
Additional notes			4 iterations 16 Subsets	Image zoom 1.5 4 iterations 16 Subsets

Dynamic reconstructions. Although the standard NEMA NU-4 protocol recommends a scan time of 20 minutes resulting in one static image, for this research, additional dynamic reconstructions with shorter frame durations have been completed in order to achieve a number of prompts per frame in the phantom scans similar to those in the rat dynamic scans. The static phantom images had an average of $3.2 \cdot 10^7$ prompts and by first lowering the frame duration to 120 seconds, a dynamic scan consisting of ten frames with an average of $3.4 \cdot 10^6$ prompts per frame was obtained. Although the number of counts was significantly lowered, it was still roughly 100 times greater than the average of the rat scans. Thus, additional dynamic scans with a frame duration of 30s were reconstructed and analysed.

Fig. 6. ROI selection for RC determination

2.2.3 Data analysis

All images were output by the scanner in .IMG format, converted to NIfTI .nii format, and ultimately analysed in ImageJ [48]. For each region, volume of interest (VOI) templates were made according to the NEMA protocol and applied to all reconstructed images. The scan was parsed and the slices containing each of the three regions were determined.

Uniformity and error. In the uniformity region, centred VOIs with a diameter of 22.5 mm, a length of 10 mm, and a volume of 3900.139 mm^3 were drawn. Using the "ROI manager" and "Measure" tools, the average activity concentration, the maximum and minimum values, and the percentage standard deviation (%SD) were extracted. Using Equation 4, the percentage error was determined.

Recovery coefficients. To determine the recovery coefficients, the first step was averaging the slides of the central 10 mm of the five rods to obtain an image with lower noise. ROIs with diameters twice the physical diameters of the rods were drawn (see Figure 6) and measured to determine the maximum pixel value for each rod and their coordinates. Afterward, line profiles along the rods were created at the locations of the maximum pixels. The pixel values along each profile were then divided by the mean activity concentration determined in the uniformity region and the resulting values were used to calculate the mean and the standard deviation of the RC for each rod diameter [16]. The percentage standard deviation (%SD) of the RC is defined as:

$$\%\mathrm{SD}_{\mathrm{RC}} = 100 \cdot \sqrt{\left(\frac{\mathrm{SD}_{\text{line profile}}}{\mathrm{Mean}_{\text{line profile}}}\right)^2 + \left(\frac{\mathrm{SD}_{\text{background}}}{\mathrm{Mean}_{\text{background}}}\right)^2} \tag{6}$$

Accuracy of corrections. VOIs were drawn in the water and air cylinders with a diameter of 4 mm and a length of 7.5 mm, covering the centre of the cylinder, and measured. The spill over ratio (SOR) and percentage standard deviations are defined as:

$$\mathrm{SOR} = \frac{\text{cold region mean activity concentration}}{\text{mean uniform activity concentration}} \tag{7}$$

$$\%\mathrm{SD}_{\mathrm{SOR}} = 100 \cdot \sqrt{\left(\frac{\mathrm{SD}_{\mathrm{cold}}}{\mathrm{Mean}_{\mathrm{cold}}}\right)^2 + \left(\frac{\mathrm{SD}_{\mathrm{uniform}}}{\mathrm{Mean}_{\mathrm{uniform}}}\right)^2} \tag{8}$$

2.3 [^{18}F]MC225 rat data study

The dataset analysed in this study was created by Garcia-Varela with the goal of assessing the brain P-glycoprotein function with [^{18}F]MC225 [21] . The following description of the acquisition procedure is in accordance with the aforementioned journal article.

2.3.1 Image acquisition procedure and Reconstruction methods

Cannulas were inserted in the femoral arteries of the rats, to collect arterial blood samples. Afterward, the animals were placed in the microPET scanner [21]. Similarly to the phantom image acquisition procedure, a 10-minute ^{57}Co transmission scan was first conducted to derive the appropriate attenuation and scatter corrections. Then, the [^{18}F]MC225 was administered and the 60-minute brain dynamic PET scan began concurrently. The list mode data were rebinned into 21 frames: 6 frames of 10 seconds, 4 frames of 30 seconds, 2 frames of 60 seconds, 1 frame of 120 seconds, 1 frame of 180 seconds, 4 frames of 300 seconds, and 3 frames of 600 seconds. All images were decay, attenuation, and scatter corrected. All sinograms were reconstructed identically the same as the phantom scans, as described in Section 2.2.2 and Table 1.

2.3.2 Blood and metabolite data acquisition

Arterial blood samples of 0.1 mL were collected sixteen times throughout the scan and saline solution was delivered to the system in quantities equal to that of the drawn blood. The blood samples were analysed using the 2480 WIZARD 2 gamma counter and the whole-blood radioactivity and plasma radioactivity were determined [37]. The radioactive metabolites were measured using thin-layer chromatography (TLC) on the plasma samples [49].

2.4 Data analysis

Time activity curves (TACs). All PET images were analysed using the PMOD v4.105 software [35]. Using the PMOD Fusion tool (PFUS), the images were co-registered through rigid matching with a dedicated [^{18}F]MC225 Wistar rat brain template (see Figure 7) [50]. Predetermined brain areas were defined as volumes of interest (VOIs) and the same template was used for the analysis of all images. The VOI template included 13 regions: amygdala, cerebellum, corpus callosum, medial geniculate, mesencephalic, septum, superior colliculus, striatum cortex, hippocampus, hypothalamus, midbrain, brainstem, thalamus, and whole brain. However, in this study, due to P-gp distribution, only the whole brain was analysed [21]. The respective brain tissue radioactivities (kBq/cc) were extracted and used to create the tissue-TACs (TACs). This process was conducted three times for each image to also evaluate the intraobserver variability, as the scan matching process is not automated.

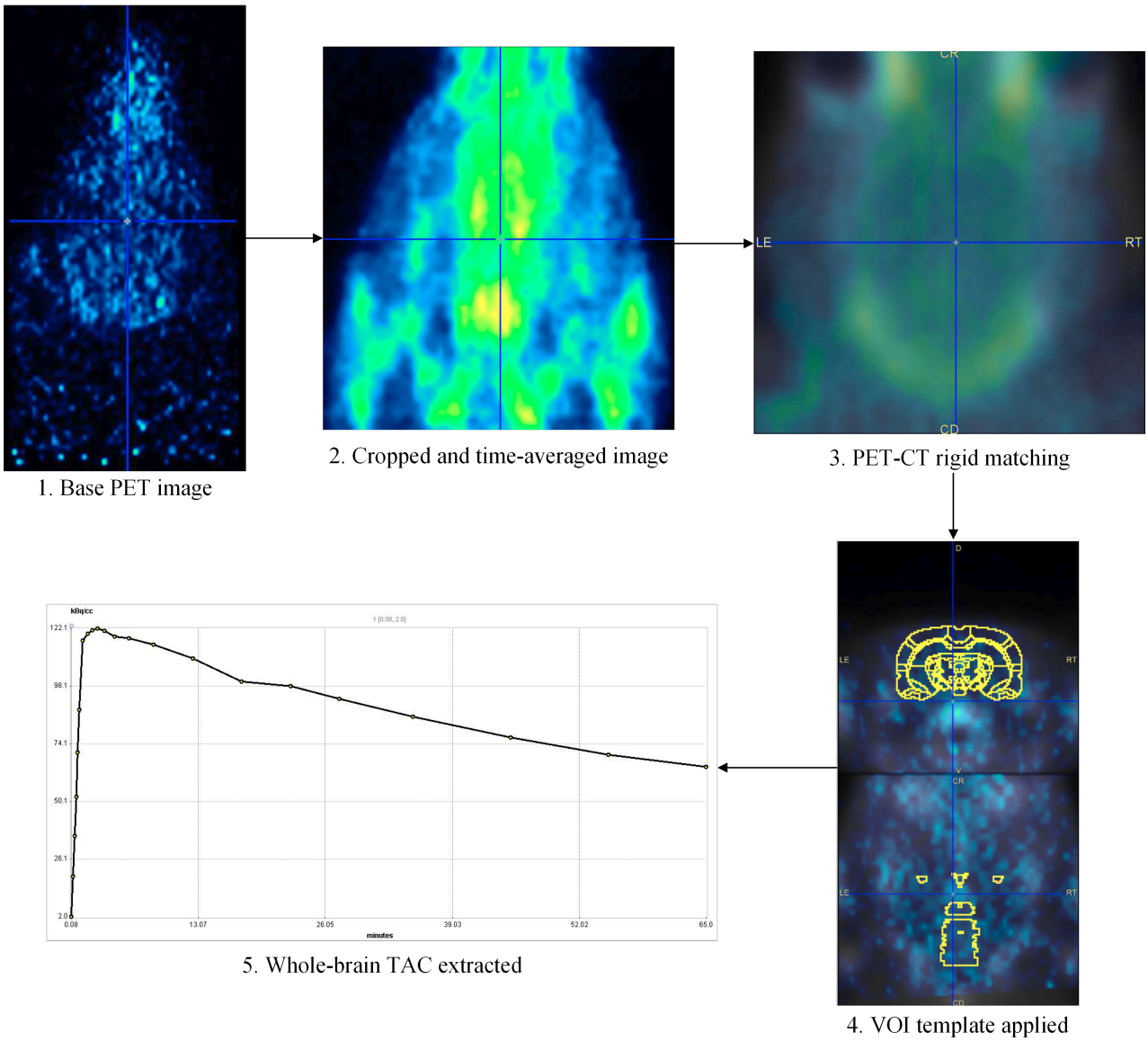

Fig. 7. TAC extraction protocol.

Kinetic modelling. The obtained TACs and the blood data were used as input for the kinetic modelling in the PMOD Kinetic Modelling tool (PKIN). As past studies have shown that the preferred model for evaluating [^{18}F]MC225 data in rats is the 1-Tissue Compartment Model (1TCM), this model was used for determining the total distribution volume V_T, the uptake rate constant K_1, and the clearance rate constant k_2 [34]. As mentioned in Section 1.1.6, the V_T represents the ratio of the radiotracer concentrations in target tissue and plasma at equilibrium and is also defined as $V_T = K_1/k_2$.

In the 1TCM at hand, the following weighting parameters were set: an unconsidered uptake, a duration equal to the frame duration, and a decay evaluated at the frame mid-time. Thus, longer and earlier acquisitions are considered the most reliable. The metabolites were fitted using a Hill function to convert the plasma activity into an input curve [51]. The blood volume fraction was fixed to 5% as recommended in previous similar literature [34].

Standard errors for each kinetic parameter were calculated using PMOD and used to evaluate the reliability of the parameter estimates. PMOD outputs the percentage standard deviation (%SE) found by multiplying the diagonal elements of the covariance matrix obtained by the fit with the Chi-square and extracting the square root [35]. The fit quality of the 1TCM for each reconstruction method image was evaluated using the Akaike information criterion (AIC), with lower values suggesting a better fit. The AIC coefficients are considered good estimates of the distance from the model to the fitted data points [52].

Statistical analysis. Unless otherwise mentioned, the TACs data are presented as mean $\pm$ standard deviation (SD), and kinetic modelling parameters K_1, k_2, and V_T are presented as mean $\pm$ standard error (SE). The statistical analysis was performed using the IBM SPSS software, version 24.0 (Armonk, NY). The differences between the TACs were analysed using Spearman correlation and the differences between the kinetic parameters groups were analysed using one-way analysis of variance (ANOVA) with Bonferroni correction. A p value < 0.050 was considered statistically significant. All plots were plotted using GraphPad Prism version 9.3.0 (San Diego, California, USA).

3 Results

3.1 Phantom study

All image quality parameters described in Section 2.2.3 have been obtained and shown in the plots and figures below.

Table 2. Mean activity concentration differences across frame durations.

Reconstruction method	Static vs 120s	Static vs 30s
FBP2D	-1.43%	-1.52%
RP3D	-0.52%	-0.23%
OSEM2D	0.00%	0.71%
OSEM2D*	1.70%	0.95%

Uniformity. The uniformity values were determined for all reconstructed scans and the image noise was quantified through the %SD (see Appendix B). The values were plotted in Figures 8 and 9 and compared, showing that the dynamic 120s RP3D, static OSEM2D*, and static OSEM2D had the least noise with very similar %SDs of 2.12%, 2.40%, and 2.54% respectively. No consistent differences were found across the frame durations for any reconstruction methods or across the reconstruction methods for any frame duration, excluding the possibility of systematic errors caused by the scanner, such as the automatic calibration factor (see Table 2).

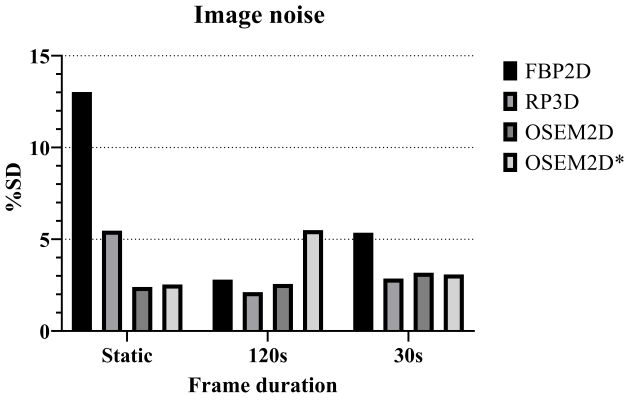

Fig. 8. Noise image (%SD) in the phantom uniformity region for all reconstruction methods.

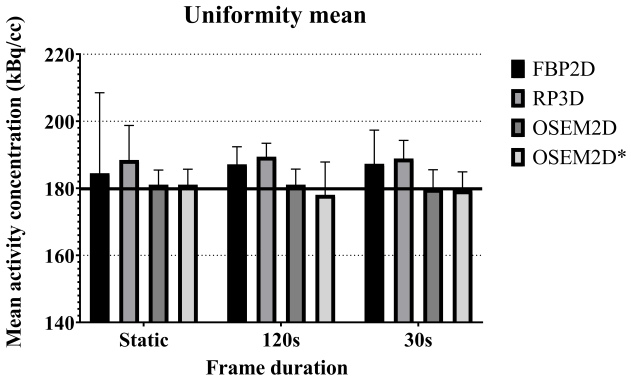

Fig. 9. Noise image (%SD) in the phantom uniformity region for all reconstruction methods.

Errors. Figure 10 shows the errors extracted using the mean activity concentrations from the uniformity region, a known activity of 179.872 kBq/cc, and Equation 4. Across all frame duration reconstructions, OSEM2D performed best with errors of 0.7% and 0.03% and RP3D performed worst with errors of 4.8%, 5.3%, and 5.1%.

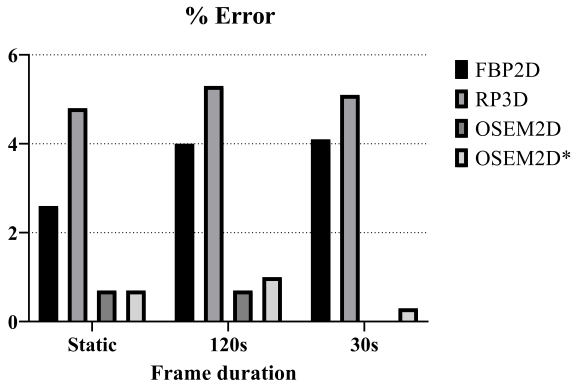

Fig. 10. Activity concentration errors of the phantom for all reconstruction methods.

Recovery coefficient. The RC values were obtained for the five hot rods of the NEMA NU-4 phantom according to Equation 3 (see Appendix C) are shown in Figure 12. The highest values for each rod diameter and frame duration were produced by the OSEM2D* and OSEM2D reconstructed images, suggesting superior performance.

The values are theoretically limited between 0 and 1, however, RCs greater than 1 were observed for both static and dynamic 120s OSEM2D and OSEM2D* reconstructed images.

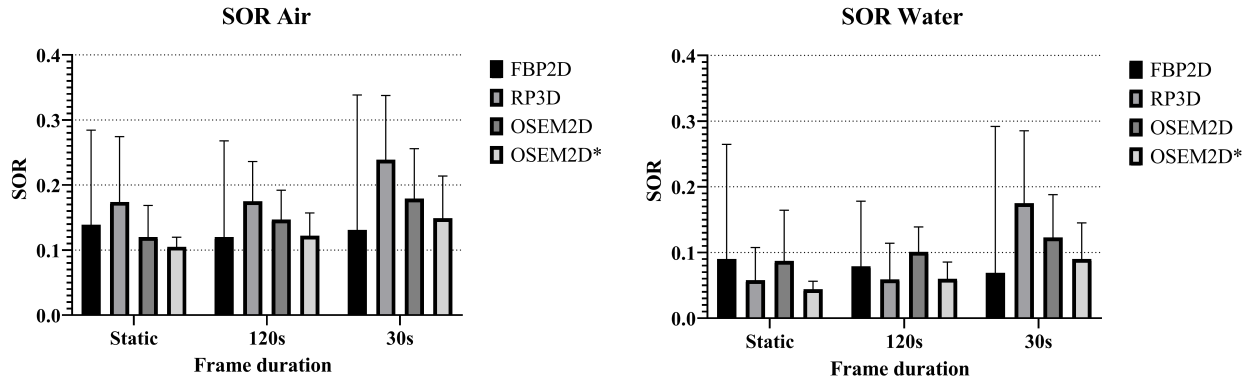

Fig. 11. Spill over ratios of the phantom for reconstruction methods.

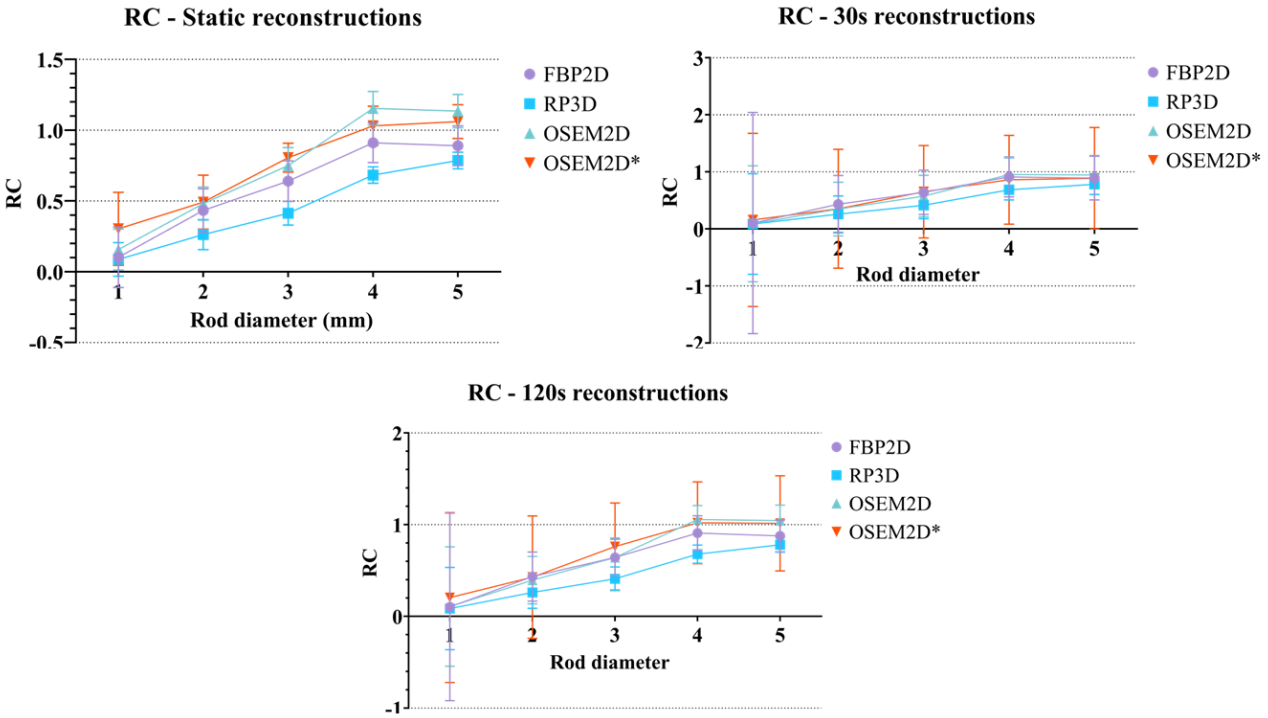

Fig. 12. RC values for all reconstruction and frame durations.

Spill over ratio. The SOR values were obtained using Equation 5 and plotted in Figure 11. The lowest SORs, indicating a better accuracy of correction, were found in the static OSEM2D* as 0.105 for air and 0.044 for water.

3.2 [^{18}F]MC225 study

Time activity curves (TACs). The time activity curves (TACs) extracted using PMOD's PFUS tool were plotted in Figure 13 and analysed using Spearman correlation. Upon visual analysis of Figure 13,

Table 3. Results for each criterion ordered best to worst performing.

Frame duration	Static		Dynamic 120s		Dynamic 30s	
Error	Reconstruction	% Error	Reconstruction	% Error	Reconstruction	% Error
	OSEM2D	0.4%	OSEM2D	0.7%	OSEM2D	0.0%
	OSEM2D*	0.7%	OSEM2D*	1.0%	OSEM2D*	0.3%
	FBP2D	2.6%	FBP2D	4.0%	FBP2D	4.1%
	RP3D	4.8%	RP3D	5.3%	RP3D	5.1%
Noise	Reconstruction	% SD	Reconstruction	% SD	Reconstruction	% SD
	OSEM2D	2.400	RP3D	2.119	RP3D	2.860
	OSEM2D*	2.538	OSEM2D	2.564	OSEM2D*	3.080
	RP3D	5.468	FBP2D	2.798	OSEM2D	3.178
	FBP2D	13.025	OSEM2D*	5.499	FBP2D	5.354
SOR Air	Reconstruction	SOR	Reconstruction	SOR	Reconstruction	SOR
	OSEM2D*	0.105	FBP2D	0.120	FBP2D	0.131
	OSEM2D	0.120	OSEM2D*	0.122	OSEM2D*	0.149
	FBP2D	0.139	OSEM2D	0.147	OSEM2D	0.179
	RP3D	0.174	RP3D	0.175	RP3D	0.239
SOR Water	Reconstruction	SOR	Reconstruction	SOR	Reconstruction	SOR
	OSEM2D*	0.044	RP3D	0.059	FBP2D	0.069
	RP3D	0.058	OSEM2D*	0.060	OSEM2D*	0.090
	OSEM2D	0.087	FBP2D	0.079	OSEM2D	0.123
	FBP2D	0.090	OSEM2D	0.101	RP3D	0.175

it can be concluded that the analytical reconstruction methods (FBP2D and RP3D) provided activity concentration values higher than the ones obtained using iterative reconstruction methods, for both rat scans. The Spearman correlation coefficients showed that there is no statistically significant difference between the TACs across reconstruction methods, as all are strongly positively correlated ($\rho > 0.943$, $p < 0.001$).

Kinetic modelling. The kinetic modelling results across the four reconstruction parameters were compared using three methods. Firstly, one-way ANOVA and Bonferroni correction were applied to all parameters to determine any statistically significant differences. The pairwise analysis showed that for the first rat, there were no significant differences between groups in K_1, k_2, and V_T. However, for the second rat, differences in K_1 were found between OSEM2D and FBP2D ($p = 0.013$), in k_2 between OSEM2D* and RP3D ($p = 0.013$), and in V_T between OSEM2D* and FBP2D ($p = 0.013$).

Secondly, the standard errors of each parameter were used to evaluate the reliability of the parameter estimates, a lower standard error signifying a better model fitting performance. In Table 4, all kinetic parameter estimates and their respective percentage standard errors can be seen. It was found across

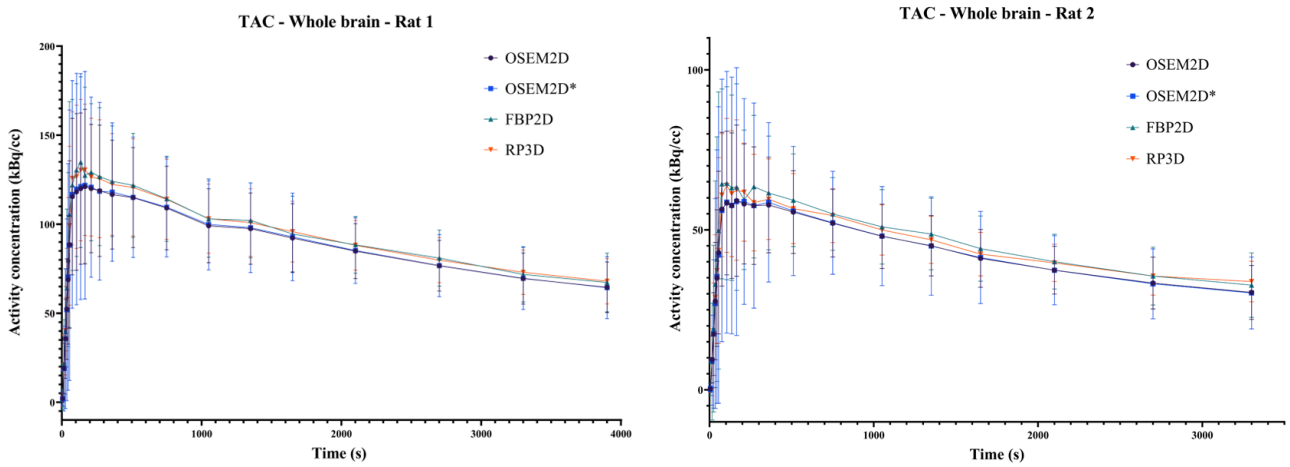

Fig. 13. Whole brain TACs of both rats.

all kinetic modelling parameters, all reconstruction protocols, and both rats that OSEM2D* had the lowest errors and highest reliability.

Table 4. Kinetic parameters results.

	Reconstruction	OSEM2D		OSEM2D*		FBP2D		RP3D	
	Parameters	Mean	%SD	Mean	%SD	Mean	%SD	Mean	%SD
Rat 1	K_1 (mL/mL/min)	0.372	2.265	0.375	2.208	0.405	2.922	0.392	2.821
	k_2 (1/min)	0.034	3.301	0.034	3.209	0.037	7.526	0.034	4.089
	V_T	11.050	1.721	11.061	1.671	11.083	5.761	11.517	2.128
Rat 2	K_1 (mL/mL/min)	0.402	1.635	0.406	1.560	0.430	2.128	0.412	2.444
	k_2 (1/min)	0.043	2.307	0.043	2.191	0.043	3.003	0.041	3.502
	V_T	9.373	1.184	9.341	1.124	10.044	1.542	10.013	1.805

Lastly, the Akaike information criterion (AIC) coefficients were computed for each kinetic model fitting and the values were compared, knowing that lower AICs signify better fitting models. As can be seen in Table 5, OSEM2D* performed best for both rat scans kinetic modelling with AIC scores of 296.47 and 252.32.

Table 5. AICs for each 1TCM fit.

Reconstruction methods		OSEM2D	OSEM2D*	FBP2D	RP3D
Rat 1	AIC	297.36	296.47	309.88	309.08
Rat 2		254.19	252.32	268.12	272.99

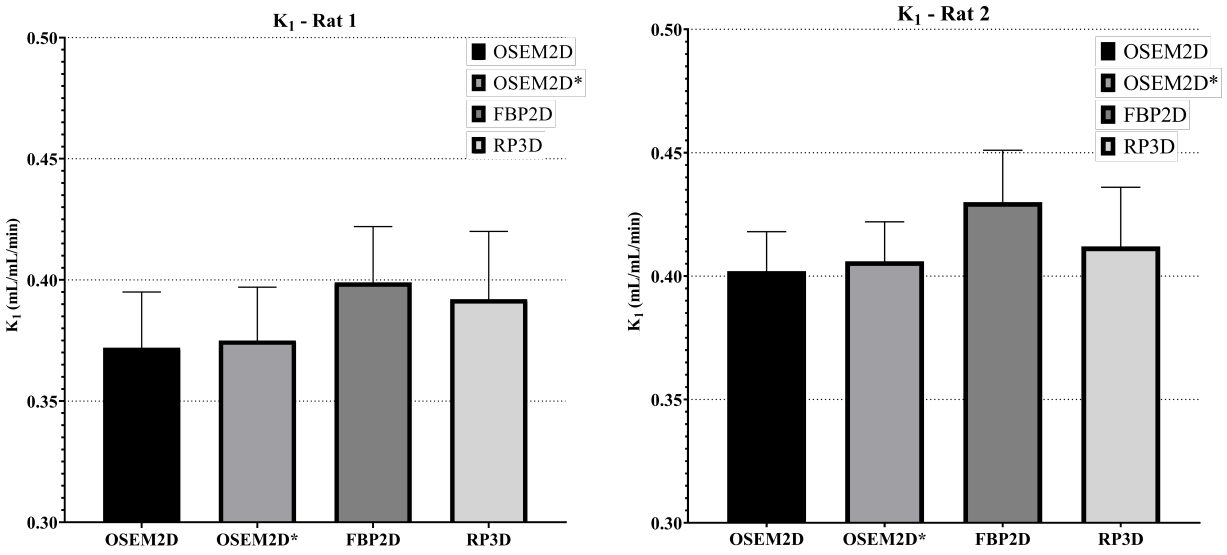

Fig. 14. K_1 kinetic parameter estimates of both rats.

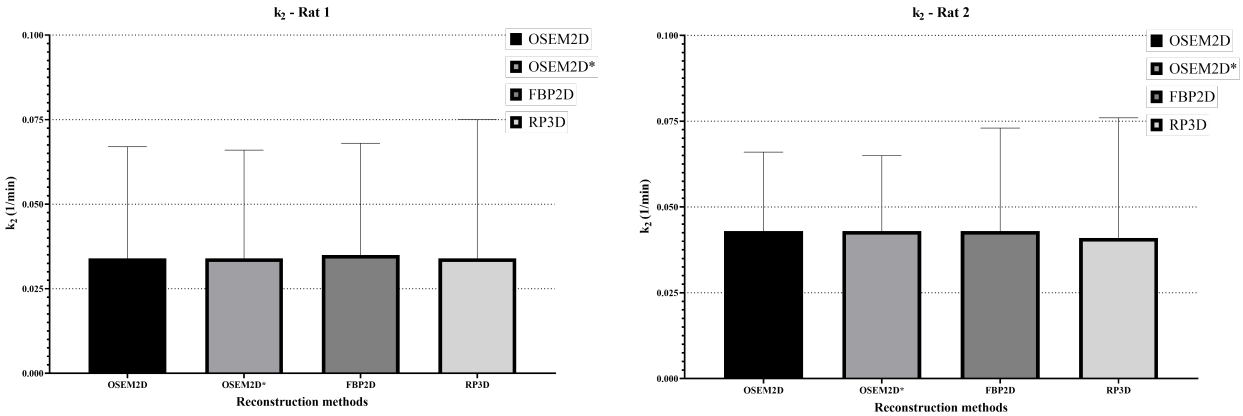

Fig. 15. k_2 kinetic parameter estimates for both rats.

4 Discussion

This study evaluated the effects of the reconstruction algorithm on image quality and addressed the effects of reconstruction methods on quantitative PET analysis methods. To discuss the results, it is divided into two sections: phantom study and [^{18}F]MC225 animal study.

4.1 Phantom study

4.1.1 IQ metrics.

Uniformity. For the uniformity segment of the phantom, dynamic 120s RP3D, static OSEM2D*, and static OSEM2D were found to perform best by noise and OSEM2D was found to perform best across all frame durations by error, reaching a minimum value of 0.03%. Upon visual analysis, an overestimation of activity concentration in analytic reconstructed images is observed.

Recovery coefficients (RCs). In this study, the RCs suggested that either OSEM2D and OSEM2D* performed best, as they achieved the highest RCs for each rod diameter across all frame durations. Moreover, overestimated RCs in the images reconstructed with static and 120s frame duration OSEM2D and OSEM2D* were observed. Plausible causes for the aforementioned overestimated RCs discussed in the literature are the Gibbs effect, image noise, and nonlinear detector response [39, 53]. The image noise, quantified using the previously discussed uniformity %SD, and the noise fluctuation can cause localised overestimations of activity concentrations, which can cause overestimated RCs. However, analysing Appendices C and B, it becomes clear that only static OSEM2D, static FBP2D, and dynamic 120s OSEM2D* reconstructed images are expected to exhibit RC values above 1, as they have the three highest uniformity %SD, which did not occur. Another factor influencing image noise are the count statistics, but all phantom scans have counts above $3 \cdot 10^6$.

Nonlinear detector response, caused by detector saturation or electronic effects, may introduce image artifacts and biases and in turn account for the overestimated RCs if the OSEM reconstruction algorithm does not correct for it appropriately. However, OSEM is known to perform better in nonlinearity corrections compared to FBP, suggesting FBP reconstructed images should be the ones exhibiting such overestimation [54]. Furthermore, it is not known whether the introduced biases and artifacts lead to activity overestimation or underestimation. Additionally, deadtime correction has been applied during the histogramming of the emission data.

Thus, the RC overestimation is in all likelihood due to the Gibbs effect, which is significantly emphasised in EM algorithms. The high contrast edges in the activity distribution become more and more prominent due to the iterative estimates causing a substantial overshoot [39, 53].

SOR. The SOR segment of the phantom showed that static OSEM2D* performed the most accurate corrections, with SORs as low as 0.105 for air and 0.044 for water, followed by FBP2D and RP3D with values of 0.120 for air and 0.058 for water, respectively.

4.1.2 Golden standard.

In order to achieve quantitative accuracy, the primary criterion for evaluating the reconstruction methods is the percentage error. Reconstruction methods with errors above 1% should not be considered

in the selection for the golden standard (Table 3). Thus, FBP2D and RP3D are not considered as their errors range between 2.6% and 5.3%. When prioritising errors, OSEM2D emerges as the best method across all frame durations. Analysing the other criteria shows that OSEM2D* and OSEM2D performed best 7 times and 5 times, respectively, per each frame duration, and 2 times each across all frame durations. However, the differences between OSEM2D and OSEM2D* are rather small across all criteria, including error.

As there are no previous studies applying the same set of reconstruction protocols on NEMA NU 4-2008 phantom scans, no direct comparison can be done. However, Disselhorst et al. compared FBP2D and OSEM2D across noise, RCs, and SORs and had differing results. It was shown that FBP2D performed better than OSEM2D across both noise and RC and very similarly across SOR. It is notable that a different microPET scanner was used and the noise values were much higher, ranging between 6% and 7.5% [39].

Furthermore, Gontijo et al. compared FBP2D and OSEM3D and found that FBP2D performed better across RCs and SORs, but OSEM3D performed best in mitigating noise. Their study also employed a different microPET scanner and reported higher noise values, ranging from 6.7% to 17.6% [38]. Lastly, McDougald et al. compared FBP2D and OSEM2D only across the RCs and found that OSEM2D performed better by producing higher coefficients for each rod diameter [40].

Based on the available evidence, it can be concluded that the most suitable reconstruction method for serving as the golden standard is OSEM2D. While the comparison with previous studies yielded varied results depending on the evaluated criteria, the collective findings suggest that OSEM2D consistently performs well and is a robust choice for achieving accurate and reliable quantitative results. However, further investigation with additional image quality metrics would be necessary to reach conclusive findings.

4.2 [^{18}F]MC225 study

4.2.1 TAC analysis

The TAC analysis conducted in Section 3.2 revealed no significant differences among the reconstruction groups. This suggests that FBP2D, RP3D, OSEM2D, and OSEM2D* yield similar quantitative results. However, it is important to note that both the RP3D and FBP2D reconstruction methods exhibited TACs with higher values compared to OSEM2D and OSEM2D*. This observation aligns with our expectations, as the NEMA phantom analysis had already indicated an overestimation of the activity concentration with the RP3D and FBP2D methods. These findings are consistent with a similar study conducted by Boellard et al. [15], which evaluated FBP2D and OSEM2D reconstructions in cardiac, oncologic, and brain dynamic scans and also found no significant differences in TACs. However, visual analysis confirmed that the RP3D and FBP2D methods indeed led to higher activity concentrations compared to OSEM2D and OSEM2D*.

4.2.2 Kinetic modelling analysis

Moreover, the analysis of the 1TCM's kinetic parameters revealed no significant differences among the reconstruction groups for the first rat. However, for the second rat, some significant differences were observed. Therefore, we cannot draw a definitive conclusion regarding how kinetic parameters are affected by the reconstruction method based on these results alone. Further investigation with a

larger sample size would be necessary to obtain more conclusive findings in this regard.

Additionally, we evaluated the performance of the 1TCM fit and compared it to the literature. The AIC values obtained were in line with those reported in previous studies, indicating that the 1TCM applied to the OSEM2D* reconstructed image performed best in terms of both the percentage standard error and AIC. These results provide further support for our initial expectations, as established by the phantom study conducted by Savolainen et al. [34].

4.3 Limitations and future prospects

A significant limitation of the study is that only two rat scans were analysed, leading to statistically inconclusive results. Furthermore, incorporating biodistribution data would help validate the microPET values and accurately determine whether any reconstruction methods produce overestimated activity concentrations. Moreover, it would be relevant to conduct a similar rat study across different radiotracers. Disselhorst et al. did perform a phantom study with additional radionuclides such as ^{68}Ga, ^{124}I, and ^{89}Zr and found that maximum a posteriori (MAP) reconstruction performed best across all radionuclides [39]. However, the effects on quantitative measurements and kinetic modelling parameters remain unknown. Lastly, the performance of the reconstruction methods on low count images remains to be studied.

5 Conclusion

The present study aimed to discuss the effects of reconstruction methods on image quality and quantitative PET analysis methods and consisted of a phantom study and an [^{18}F]MC225 animal study. The findings of the phantom study suggest that OSEM2D performs best and OSEM2D* performs very similarly across all image quality metrics. However, the available data is limited and appears to contradict previous studies, requiring further investigation. The [^{18}F]MC225 animal study found no significant differences across tissue time-activity curves across reconstruction methods and some significant differences across some kinetic model parameters, but not all. Furthermore, the model fit analysis suggested that the 1-tissue compartment model fit best on OSEM2D* reconstructed images. Due to the limited sample size, additional investigation is necessary to obtain a definitive answer.

References

[1] Anna Schildt. "PET methodology in rat models of Parkinson's disease". en. ISBN: 9789403426266. PhD thesis. University of Groningen, May 2020. DOI: 10.33612/diss.125440245.

[2] Ilaria Grassi et al. "The clinical use of PET with (11)C-acetate". eng. In: *American Journal of Nuclear Medicine and Molecular Imaging* 2.1 (2012), pp. 33–47. ISSN: 2160-8407.

[3] Gengsheng Lawrence Zeng. *Medical image reconstruction: a conceptual tutorial*. eng. Berlin: Springer, 2010. ISBN: 978-7-04-020437-7 978-3-642-05367-2.

[4] DJ Schlyer. "PET Tracers and Radiochemistry". en. In: 33.2 (2004).

[5] Kristina Herfert et al. "Quantitative Rodent Brain Receptor Imaging". en. In: *Molecular Imaging and Biology* 22.2 (Apr. 2020), pp. 223–244. ISSN: 1536-1632, 1860-2002. DOI: 10.1007/s11307-019-01368-9.

[6] A. F. Chatziioannou. "Instrumentation for Molecular Imaging in Preclinical Research: Micro-PET and Micro-SPECT". en. In: *Proceedings of the American Thoracic Society* 2.6 (Dec. 2005), pp. 533–536. ISSN: 1546-3222. DOI: 10.1513/pats.200508-079DS.

[7] Sophie Lancelot and Luc Zimmer. "Small-animal positron emission tomography as a tool for neuropharmacology". en. In: *Trends in Pharmacological Sciences* 31.9 (Sept. 2010), pp. 411–417. ISSN: 01656147. DOI: 10.1016/j.tips.2010.06.002.

[8] Wade Koba, Linda A. Jelicks, and Eugene J. Fine. "MicroPET/SPECT/CT Imaging of Small Animal Models of Disease". en. In: *The American Journal of Pathology* 182.2 (Feb. 2013), pp. 319–324. ISSN: 00029440. DOI: 10.1016/j.ajpath.2012.09.025.

[9] Jürgen K. Willmann et al. "Molecular imaging in drug development". en. In: *Nature Reviews Drug Discovery* 7.7 (July 2008), pp. 591–607. ISSN: 1474-1776, 1474-1784. DOI: 10.1038/nrd2290.

[10] Lídia Cunha et al. "Preclinical Imaging: an Essential Ally in Modern Biosciences". en. In: *Molecular Diagnosis & Therapy* 18.2 (Apr. 2014), pp. 153–173. ISSN: 1177-1062, 1179-2000. DOI: 10.1007/s40291-013-0062-3.

[11] S. R. Cherry and S. S. Gambhir. "Use of Positron Emission Tomography in Animal Research". en. In: *ILAR Journal* 42.3 (Jan. 2001), pp. 219–232. ISSN: 1084-2020. DOI: 10.1093/ilar.42.3.219.

[12] E. Herranz et al. "Quantification limits of iterative PET reconstruction algorithms and improved estimation of kinetic constants". In: *2011 IEEE Nuclear Science Symposium Conference Record*. Valencia, Spain: IEEE, Oct. 2011, pp. 2968–2972. ISBN: 978-1-4673-0120-6 978-1-4673-0118-3 978-1-4673-0119-0. DOI: 10.1109/NSSMIC.2011.6152530.

[13] Julian M. M. Rogasch et al. "Influences on PET Quantification and Interpretation". en. In: *Diagnostics* 12.2 (Feb. 2022), p. 451. ISSN: 2075-4418. DOI: 10.3390/diagnostics12020451.

[14] J Hove et al. "Clinical evaluation of iterative reconstruction (ordered-subset expectation maximization) in dynamic positron emission tomography: Quantitative effects on kinetic modeling with N-13 ammonia in healthy subjects". en. In: *Journal of Nuclear Cardiology* 15.4 (July 2008), pp. 530–534. ISSN: 10713581. DOI: 10.1016/j.nuclcard.2008.02.034.

[15] R. Boellaard, A. van Lingen, and A. A. Lammertsma. "Experimental and clinical evaluation of iterative reconstruction (OSEM) in dynamic PET: quantitative characteristics and effects on kinetic modeling". eng. In: *Journal of Nuclear Medicine: Official Publication, Society of Nuclear Medicine* 42.5 (May 2001), pp. 808–817. ISSN: 0161-5505.

[16] National Electrical Manufacturers Association. "Performance Measurements of Small Animal Positron Emission Tomographs". In: *2008 Standards Publication NU 4- (2008)* (Dec. 2011).

[17] Magdy M. Khalil, ed. *Basic Science of PET Imaging*. en. Cham: Springer International Publishing, 2017. ISBN: 978-3-319-40068-6 978-3-319-40070-9. DOI: 10.1007/978-3-319-40070-9.

[18] Gert Luurtsema et al. "PET Tracers for Imaging of ABC Transporters at the Blood-Brain Barrier: Principles and Strategies". en. In: *Current Pharmaceutical Design* 22.38 (Nov. 2016), pp. 5779–5785. ISSN: 13816128. DOI: 10.2174/1381612822666160810123634.

[19] Ronald Boellaard et al. "FDG PET/CT: EANM procedure guidelines for tumour imaging: version 2.0". en. In: *European Journal of Nuclear Medicine and Molecular Imaging* 42.2 (Feb. 2015), pp. 328–354. ISSN: 1619-7070, 1619-7089. DOI: 10.1007/s00259-014-2961-x.

[20] Fabio Fusi et al. "MC225, a Novel Probe for P-glycoprotein PET Imaging at the Blood–brain Barrier: In Vitro Cardiovascular Safety Evaluation". en. In: *Journal of Cardiovascular Pharmacology* 70.6 (Dec. 2017), pp. 405–410. ISSN: 0160-2446. DOI: 10.1097/FJC.0000000000000536.

[21] Lara Garcia-Varela et al. "Dose-response assessment of cerebral P-glycoprotein inhibition in vivo with [18F]MC225 and PET". en. In: *Journal of Controlled Release* 347 (July 2022), pp. 500–507. ISSN: 01683659. DOI: 10.1016/j.jconrel.2022.05.026.

[22] Todd Faasse. "Positron Emission Tomography-Computed Tomography Data Acquisition and Image Management". en. In: *Positron Emission Tomography - Recent Developments in Instrumentation, Research and Clinical Oncological Practice*. Ed. by Sandro Misciagna. InTech, Dec. 2013. ISBN: 978-953-51-1213-6. DOI: 10.5772/57119.

[23] F. M. Ribeiro et al. "A guideline proposal for mice preparation and care in 18F-FDG PET imaging". en. In: *EJNMMI Research* 12.1 (Aug. 2022), p. 49. ISSN: 2191-219X. DOI: 10.1186/s13550-022-00921-y.

[24] Valentin Duclos et al. "PET Molecular Imaging: A Holistic Review of Current Practice and Emerging Perspectives for Diagnosis, Therapeutic Evaluation and Prognosis in Clinical Oncology". en. In: *International Journal of Molecular Sciences* 22.8 (Apr. 2021), p. 4159. ISSN: 1422-0067. DOI: 10.3390/ijms22084159.

[25] Gabriele Tarantola, Felicia Zito, and Paolo Gerundini. "PET Instrumentation and Reconstruction Algorithms in Whole-Body Applications". en. In: *Journal of Nuclear Medicine* 44.5 (May 2003). ISSN: 0161-5505.

[26] Michel Defrise and Paul Kinahan. "Data Acquisition and Image Reconstruction for 3D PET". en. In: *The Theory and Practice of 3D PET*. Ed. by Bernard Bendriem and David W. Townsend. Dordrecht: Springer Netherlands, 1998, pp. 11–53. ISBN: 978-90-481-5040-3 978-94-017-3475-2. DOI: 10.1007/978-94-017-3475-2_2.

[27] Andrew J. Reader and Habib Zaidi. "Advances in PET Image Reconstruction". en. In: *PET Clinics* 2.2 (Apr. 2007), pp. 173–190. ISSN: 15568598. DOI: 10.1016/j.cpet.2007.08.001.

[28] G. Mettivier et al. “The effect of count statistics on the convergence value in OSEM reconstruction in PET and TOF PET”. In: *2011 IEEE Nuclear Science Symposium Conference Record*. Valencia: IEEE, Oct. 2011, pp. 2400–2406. ISBN: 978-1-4673-0118-3 978-1-4673-0120-6. DOI: 10.1109/NSSMIC.2011.6152654.

[29] Y Jian, B Planeta, and R E Carson. “Evaluation of bias and variance in low-count OSEM list mode reconstruction”. en. In: *Physics in Medicine and Biology* 60.1 (Jan. 2015), pp. 15–29. ISSN: 0031-9155, 1361-6560. DOI: 10.1088/0031-9155/60/1/15.

[30] Ronald Boellaard, Arthur van Lingen, and Adriaan A Lammertsma. “Experimental and Clinical Evaluation of Iterative Reconstruction (OSEM) in Dynamic PET: Quantitative Characteristics and Effects on Kinetic Modeling”. en. In: *Journal of Nuclear Medicine* 42.5 (May 2001). ISSN: 0161-5505.

[31] Ximin Shi et al. “Comparison among Reconstruction Algorithms for Quantitative Analysis of ^{11} C-Acetate Cardiac PET Imaging”. en. In: *Contrast Media & Molecular Imaging* 2018 (2018), pp. 1–10. ISSN: 1555-4309, 1555-4317. DOI: 10.1155/2018/9193403.

[32] R Buchert et al. *PET Pharmacokinetics Course Manual*. Ed. by Jorg van den Hoff and R.P. Maguire. Dresden, Germany, Mar. 2017.

[33] Steven R Meikle et al. “Quantitative PET in the 2020s: a roadmap”. en. In: *Physics in Medicine & Biology* 66.6 (Mar. 2021), 06RM01. ISSN: 0031-9155, 1361-6560. DOI: 10.1088/1361-6560/abd4f7.

[34] Heli Savolainen et al. “Evaluation of [^{18} F]MC225 as a PET radiotracer for measuring P-glycoprotein function at the blood–brain barrier in rats: Kinetics, metabolism, and selectivity”. en. In: *Journal of Cerebral Blood Flow & Metabolism* 37.4 (Apr. 2017), pp. 1286–1298. ISSN: 0271-678X, 1559-7016. DOI: 10.1177/0271678X16654493.

[35] PMOD Technologies. *PMOD*. Zurich, Switzerland.

[36] *VDC-505 Dose Calibrator*.

[37] *Wizard2 1-Detector Gamma Counter, 3 inches: 2480-0010 — PerkinElmer*.

[38] Rodrigo M G Gontijo et al. “Image Quality Assesment using NEMA NU 4/2008 Standards in Small Animal PET Scanner”. en. In: *Brazilian Journal of Radiation Sciences* 7 (Feb. 2019). DOI: 10.15392/bjrs.v7i2A.580.

[39] Jonathan A. Disselhorst et al. “Image-Quality Assessment for Several Positron Emitters Using the NEMA NU 4-2008 Standards in the Siemens Inveon Small-Animal PET Scanner”. en. In: *Journal of Nuclear Medicine* 51.4 (Apr. 2010), pp. 610–617. ISSN: 0161-5505, 2159-662X. DOI: 10.2967/jnumed.109.068858.

[40] Wendy McDougald et al. “Standardization of Preclinical PET/CT Imaging to Improve Quantitative Accuracy, Precision, and Reproducibility: A Multicenter Study”. en. In: *Journal of Nuclear Medicine* 61.3 (Mar. 2020), pp. 461–468. ISSN: 0161-5505, 2159-662X. DOI: 10.2967/jnumed.119.231308.

[41] Julia G. Mannheim et al. “Reproducibility and Comparability of Preclinical PET Imaging Data: A Multicenter Small-Animal PET Study”. en. In: *Journal of Nuclear Medicine* 60.10 (Oct. 2019), pp. 1483–1491. ISSN: 0161-5505, 2159-662X. DOI: 10.2967/jnumed.118.221994.

[42] Mahsa Amirrashedi et al. “NEMA NU-4 2008 performance evaluation of Xtrim-PET: A prototype SiPM-based preclinical scanner”. en. In: *Medical Physics* 46.11 (Nov. 2019), pp. 4816–4825. ISSN: 0094-2405, 2473-4209. DOI: 10.1002/mp.13785.

[43] Silje Kjærnes Øen et al. “Image quality and detectability in Siemens Biograph PET/MRI and PET/CT systems—a phantom study”. en. In: *EJNMMI Physics* 6.1 (Dec. 2019), p. 16. ISSN: 2197-7364. DOI: 10.1186/s40658-019-0251-1.

[44] Hyeon-Sik Kim, Byeong-il Lee, and Jae-Sung Ahn. “Assessment of MicroPET Image Quality Based on Reconstruction Methods and Post-Filtering”. en. In: *Applied Sciences* 11.18 (Sept. 2021), p. 8707. ISSN: 2076-3417. DOI: 10.3390/app11188707.

[45] Andrew L. Goertzen et al. “NEMA NU 4-2008 Comparison of Preclinical PET Imaging Systems”. en. In: *Journal of Nuclear Medicine* 53.8 (Aug. 2012), pp. 1300–1309. ISSN: 0161-5505, 2159-662X. DOI: 10.2967/jnumed.111.099382.

[46] Rameshwar Prasad, Osman Ratib, and Habib Zaidi. “NEMA NU-04-based performance characteristics of the LabPET-8™ small animal PET scanner”. en. In: *Physics in Medicine and Biology* 56.20 (Oct. 2011), pp. 6649–6664. ISSN: 0031-9155, 1361-6560. DOI: 10.1088/0031-9155/56/20/009.

[47] Weidong Luo, Edward Anashkin, and Christopher G. Matthews. “Performance Evaluation of a PEM Scanner Using the NEMA NU 4—2008 Small Animal PET Standards”. en. In: *IEEE Transactions on Nuclear Science* 57.1 (Feb. 2010), pp. 94–103. ISSN: 0018-9499, 1558-1578. DOI: 10.1109/TNS.2009.2036847.

[48] Caroline A Schneider, Wayne S Rasband, and Kevin W Eliceiri. “NIH Image to ImageJ: 25 years of image analysis”. en. In: *Nature Methods* 9.7 (July 2012), pp. 671–675. ISSN: 1548-7091, 1548-7105. DOI: 10.1038/nmeth.2089.

[49] Lara García-Varela et al. “Test–Retest Repeatability of [^{18} F]MC225-PET in Rodents: A Tracer for Imaging of P-gp Function”. en. In: *ACS Chemical Neuroscience* 11.4 (Feb. 2020), pp. 648–658. ISSN: 1948-7193, 1948-7193. DOI: 10.1021/acschemneuro.9b00682.

[50] David Vállez Garcia et al. “A Standardized Method for the Construction of Tracer Specific PET and SPECT Rat Brain Templates: Validation and Implementation of a Toolbox”. en. In: *PLOS ONE* 10.3 (Mar. 2015). Ed. by Jean-Claude Baron, e0122363. ISSN: 1932-6203. DOI: 10.1371/journal.pone.0122363.

[51] Roger N. Gunn et al. “Tracer Kinetic Modeling of the 5-HT1AReceptor Ligand [carbonyl-11C]WAY-100635 for PET”. en. In: *NeuroImage* 8.4 (Nov. 1998), pp. 426–440. ISSN: 10538119. DOI: 10.1006/nimg.1998.0379.

[52] Federico E. Turkheimer, Rainer Hinz, and Vincent J. Cunningham. “On the Undecidability among Kinetic Models: From Model Selection to Model Averaging”. en. In: *Journal of Cerebral Blood Flow & Metabolism* 23.4 (Apr. 2003), pp. 490–498. ISSN: 0271-678X, 1559-7016. DOI: 10.1097/01.WCB.0000050065.57184.BB.

[53] Donald L. Snyder et al. “Noise and Edge Artifacts in Maximum-Likelihood Reconstructions for Emission Tomography”. en. In: *IEEE Transactions on Medical Imaging* 6.3 (Sept. 1987), pp. 228–238. ISSN: 0278-0062, 1558-254X. DOI: 10.1109/TMI.1987.4307831.

[54] Simon R. Cherry and Magnus Dahlbom. “PET: Physics, Instrumentation, and Scanners”. en. In: *PET*. Ed. by Michael E. Phelps. New York, NY: Springer New York, 2006, pp. 1–117. ISBN: 978-0-387-32302-2. DOI: 10.1007/0-387-34946-4_1.

Appendices

A Phantom slices

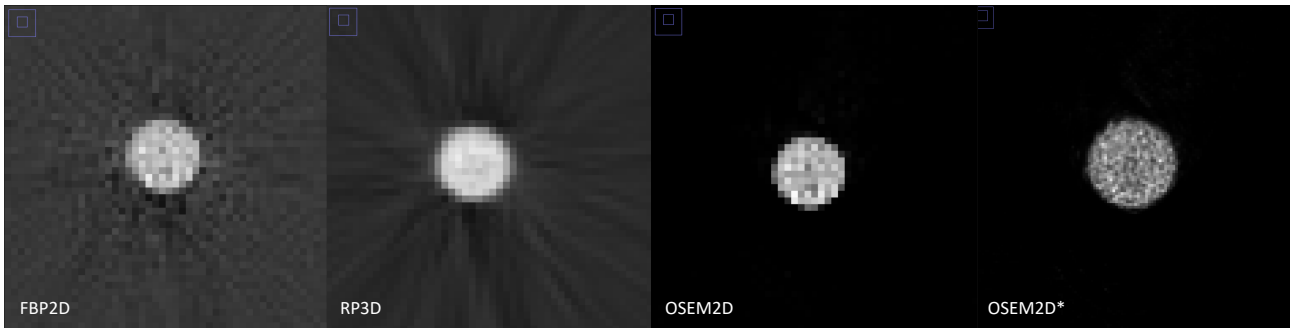

Transverse static plane images of the phantom uniform region.

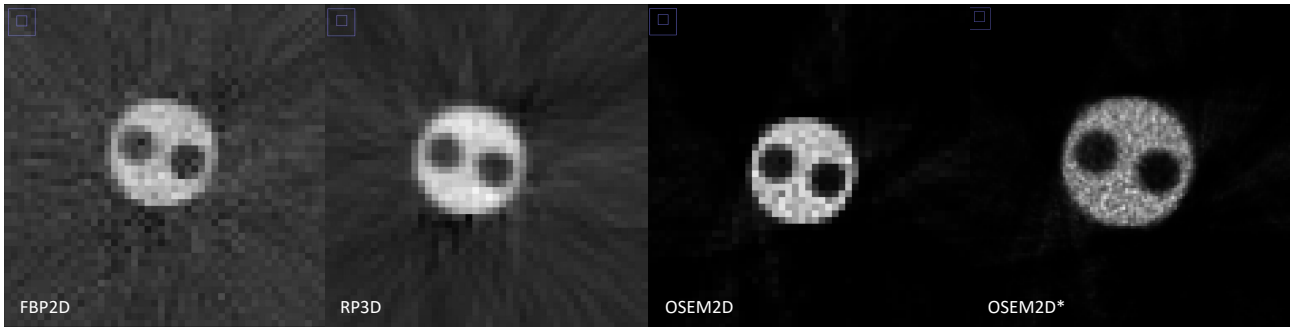

Transverse static plane images of the phantom spill over ratio region.

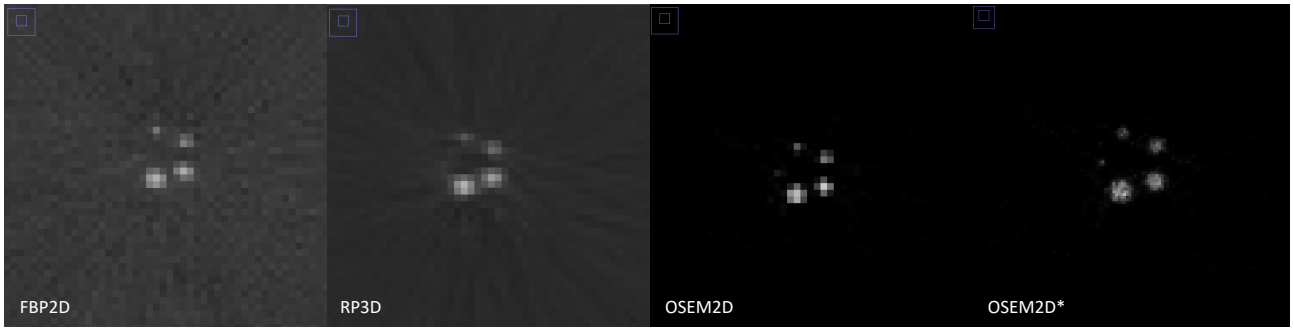

Transverse static plane images of the phantom recovery coefficient region.

B Phantom uniformity, percentage error, and accuracy of corrections (SOR)

Frame duration	Uniformity					% Error	Accuracy of corrections			
							Region			
							Air cylinder		Water cylinder	
	Reconstruction method	Mean	Maximum	Minimum	%SD		SOR	%SD	SOR	%SD
Static	**FBP2D**	184.487	264.107	98.342	13.02	2.6%	0.139	104.57	0.090	193.47
	RP3D	188.450	222.135	160.383	5.47	4.8%	0.174	57.54	0.058	85.05
	OSEM2D	181.093	243.553	121.809	2.40	0.7%	0.120	40.50	0.087	88.91
	OSEM2D*	181.093	297.258	98.132	2.54	0.7%	0.105	14.11	0.044	27.52
Dynamic 120s	**FBP2D**	187.156	422.454	-24.067	2.80	4.0%	0.120	123.59	0.079	124.93
	RP3D	189.444	282.336	85.879	2.12	5.3%	0.175	35.02	0.059	93.33
	OSEM2D	181.102	387.520	34.228	2.56	0.7%	0.147	30.63	0.101	37.65
	OSEM2D*	178.062	691.800	13.942	5.50	1.0%	0.122	28.78	0.060	42.52
Dynamic 30s	**FBP2D**	187.327	707.670	-292.006	5.35	4.1%	0.131	158.91	0.069	322.74
	RP3D	188.893	411.646	-34.770	2.86	5.1%	0.239	41.38	0.175	62.88
	OSEM2D	179.817	719.399	2.376	3.18	0.03%	0.179	42.97	0.123	52.83
	OSEM2D*	179.381	1463.782	0.681	3.08	0.3%	0.149	43.38	0.090	61.17

C Phantom recovery coefficients (RC)

Frame duration	Reconstruction method	Recovery coefficients									
		Rod diameter									
		1mm		2mm		3mm		4mm		5mm	
		RC	%SD	RC	%SD	RC	%SD	RC	%SD	RC	%SD
Static	FBP2D	0.107	21.33	0.440	15.32	0.653	14.28	0.921	14.01	0.892	14.09
	RP3D	0.087	11.85	0.263	10.68	0.413	8.38	0.683	5.82	0.786	5.86
	OSEM2D	0.157	14.39	0.481	11.72	0.750	12.70	1.154	11.93	1.135	11.77
	OSEM2D*	0.303	25.79	0.492	19.05	0.806	10.23	1.031	13.88	1.061	11.93
Dynamic 120s	FBP2D	0.103	102.26	0.434	26.76	0.643	19.81	0.909	18.77	0.878	17.19
	RP3D	0.085	44.87	0.261	17.28	0.410	12.93	0.679	9.94	0.781	8.24
	OSEM2D	0.107	65.04	0.395	25.93	0.642	21.37	1.056	15.24	1.044	16.90
	OSEM2D*	0.205	92.62	0.428	66.70	0.762	47.43	1.020	44.63	1.015	51.83
Dynamic 30s	FBP2D	0.102	193.83	0.433	50.44	0.640	38.87	0.911	35.06	0.890	38.381
	RP3D	0.086	88.24	0.259	31.89	0.414	23.62	0.685	17.90	0.782	17.995
	OSEM2D	0.090	101.67	0.347	47.00	0.575	36.55	0.952	29.11	0.945	34.154
	OSEM2D*	0.157	151.84	0.353	104.28	0.651	81.01	0.861	77.80	0.887	89.011